

ABSTRACT

Annular patterns with a high degree of zonal symmetry play a prominent role in the natural variability of the atmospheric circulation and its response to external forcing. But despite their apparent importance for understanding climate variability, the processes that give rise to their marked zonally symmetric components remain largely unclear.

Here the authors use simple stochastic models in conjunction with atmospheric model and observational analyses to explore the conditions under which annular patterns arise from Empirical Orthogonal Function (EOF) analysis of the flow. The results indicate that annular patterns arise not only from zonally coherent fluctuations in the circulation, i.e., “dynamical annularity”, but also from zonally symmetric statistics of the circulation in the absence of zonally coherent fluctuations, i.e., “statistical annularity”. It is argued that the distinction between dynamical and statistical annular patterns derived from EOF analysis can be inferred from the associated variance spectrum: larger differences in the variance explained by an annular EOF and successive EOFs generally indicate underlying dynamical annularity.

The authors provide a simple recipe for assessing the conditions that give rise to annular EOFs of the circulation. When applied to numerical models, the recipe indicates dynamical annularity in parameter regimes with strong feedbacks between the eddies and mean flow. When applied to observations, the recipe indicates that annular EOFs generally derive from statistical annularity of the flow in the middle latitude troposphere, but from dynamical annularity in both the stratosphere and the mid-high latitude Southern Hemisphere troposphere.

1. Introduction

“Annular” patterns of variability are structures dominated by their zonally symmetric components. They emerge as the leading empirical orthogonal functions (EOFs) of the Northern Hemisphere sea-level pressure field (Lorenz 1951; Kutzbach 1970; Wallace and Gutzler 1981; Trenberth and Paolino 1981; Thompson and Wallace 1998, 2000), the Southern Hemisphere zonal-wind and geopotential height fields (Kidson 1988; Karoly 1990; Hartmann and Lo 1998; Thompson and Wallace 2000; Lorenz and Hartmann 2001), the Southern Hemisphere eddy-kinetic field (Thompson and Woodworth 2014), the extratropical circulation in a hierarchy of numerical simulations of the atmospheric circulation (e.g., Robinson 1991; Yu and Hartmann 1993; Lee and Feldstein 1996; Shindell et al. 1999; Gerber and Vallis 2007), and aquaplanet simulations of the ocean circulation (Marshall et al. 2007). They are seemingly ubiquitous features in a range of geophysical flows.

Despite their ubiquity in the climate system, one key aspect of annular structures remains open to debate: What gives rise to their marked zonally symmetric components? Does the zonal symmetry of annular structures reflect coherent variations in climate across a range of longitudes? Or does it largely reflect the constraints of EOF analysis (e.g., Dommenges and Latif 2002; Gerber and Vallis 2005)? Consider a long-standing example: the so-called northern annular mode (NAM) emerges as the leading EOF of the NH sea-level pressure field (e.g., Thompson and Wallace 2000). It exhibits a high degree of zonal symmetry and its structure implies in-phase variability in climate between the North Atlantic and North Pacific sectors of the hemisphere. But as discussed extensively in earlier papers (e.g., Deser 2000; Ambaum et al. 2001), the two primary centers of action of the NAM do not exhibit robust correlations on month-to-month timescales. Does the annularity of the NAM arise from dynamic connections between widely separated longitudes that are simply masked by other forms of variability (e.g., Wallace and Thompson 2002)? Or does the annularity arise from the constraints of the EOF analysis (e.g., Dommenges and Latif 2002; Gerber and Vallis 2005)?

53 The purpose of this paper is to revisit the conditions that give rise to annular structures
54 in the leading patterns of variability of the circulation. We will demonstrate that annular
55 patterns can arise from two distinct characteristics of the flow: (i) “dynamical annularity”,
56 where variability in the circulation about its mean state exhibits in-phase correlations at all
57 longitudes, and (ii) “statistical annularity”, where the statistics of the flow (e.g., the variance,
58 autocorrelation and spatial decorrelation scale) are similar at all longitudes. Both conditions
59 can give rise to annular-like EOFs that make important contributions to the variability in
60 the circulation. But only the former corresponds to coherent annular motions in the flow.
61 Section 2 explores the impacts of “dynamical annularity” vs. “statistical annularity” on
62 EOF analysis of output from two simple stochastic models. Section 3 provides theoretical
63 context for interpreting the results of the simple models. Section 4 applies the insights
64 gained from the simple models to the circulation of an idealized general circulation model
65 and observations. Conclusions are provided in Section 5.

66 2. A Tale of Two Annular Modes

67 In the following, we will define *dynamical annularity* as the case where there are positive
68 covariances between all longitudes around the globe, i.e.,

$$\text{cov}_X(\lambda_1, \lambda_2) = \frac{\sum_{n=1}^N X(\lambda_1, t_n)X(\lambda_2, t_n)}{N} > 0 \quad (1)$$

69 for all longitudes λ_1 and λ_2 . With this notation, we take X to be a generic variable of interest
70 (e.g., geopotential height or eddy kinetic energy), given as an anomaly from its climatological
71 mean. If (1) is satisfied, there are coherent underlying motions which cause the circulation
72 to vary in concert at all longitudes. We will define *statistical annularity* as the case where
73 the statistics of the flow do not vary as a function of longitude, i.e.,

$$\text{cov}_X(\lambda_1, \lambda_2) = f(\Delta\lambda). \quad (2)$$

74 where $\Delta\lambda = |\lambda_1 - \lambda_2|$ is the absolute distance between the two points. This definition
75 implies that the variance of the flow is uniform, i.e. $f(0)$, and the covariance between any
76 two longitudes depends only on the distance between them, but not where the two points
77 lie relative to the origin (prime meridian). These criteria are not mutually exclusive, and a
78 flow could satisfy both criteria at once. One would only expect (2) to hold approximately in
79 the presence of realistic boundary conditions, but in Section 4 we show the statistics of the
80 observed atmosphere are remarkably annular, particularly in the Southern Hemisphere.

81 Here we illustrate how statistical annularity can give rise to an annular EOF, even in
82 the case where there is no underlying dynamical annularity in the circulation (that is, the
83 motions are explicitly local). We consider two 1-dimensional stochastic models, $X_1(\lambda, j)$
84 and $X_2(\lambda, j)$. The details of the models are given in the Appendix, but all the necessary
85 statistics of the models are summarized in Fig. 1. In short, both models are random processes
86 in longitude, are periodic over 360° , and have zonally uniform statistics (2). The distinction
87 between the models lies in their covariance structures (Fig. 1c). For model X_1 , there is
88 explicitly no global correlation: variability at a given location is only correlated with other
89 longitudes over a range of about $\pm 90^\circ$. For model X_2 there is a global correlation of 0.1.

90 Note that since both models have zonally uniform statistics, the covariance structures
91 shown in Fig. 1c are independent of the base longitude used in the calculations. Moreover,
92 they contain all the information needed to characterize the EOFs of the two models; recall
93 that EOFs correspond to the eigenvectors of the covariance matrix $c_{ij} = \text{cov}_X(\lambda_i, \lambda_j)$. When
94 the statistics are uniform, c_{ij} is simply a function of the distance between λ_i and λ_j , as
95 illustrated in Fig. 1c.

96 The top three EOFs for the two models are shown in Fig. 2a and b. By construction (see
97 discussion in the next section), both models exhibit exactly the same EOFs. The first EOF
98 is perfectly annular, as the analytic formulation of the model allows us to take the limit of
99 infinite sampling. As seen in Fig. 2c, the first EOF also explains exactly the same fraction
100 of the variance in each model: 20%. The second and third EOFs characterize wavenumber 1

101 anomalies: all higher order EOFs come in sinusoidal pairs, increasing in wavenumber. The
102 phase is arbitrary, as the two wavenumber 1 modes explain the same fraction of variance. For
103 finite sampling, one would see slight mixing between the wavenumbers, but the top modes
104 are well established, even for a reasonable number of samples.

105 The key result in Fig. 2 is that both models exhibit a robust “annular mode” as their
106 leading EOF, and that both annular modes explain the same total fraction of the variance.
107 Only one of the apparent “annular modes”, however, reflects dynamical annularity in the
108 flow.

109 From the perspective of EOFs, one can only distinguish the two models by examining
110 their EOF spectra, i.e., the relative variance associated with all modes (Fig. 2c). By design,
111 the annular modes (the leading EOFs) in both models explain the same fraction of the total
112 variance (20%). The key differences between the EOF spectra from the two models lie in the
113 relative variance explained by their higher order EOFs. In the case of model 1, the first EOF
114 explains only slightly more variance than the second or third EOFs. In the case of model 2,
115 there is a large gap between the first and second EOFs. It is the relative variance explained
116 that provides insight into the relative importance of statistical vs. dynamical annularity in
117 giving rise to an annular-like leading EOF.

118 The stochastic models considered in Figs. 1 and 2 highlight two key aspects of annular
119 modes. First the models make clear that identical annular-like patterns can arise from two
120 very different configurations of the circulation: (i) cases where the statistics of the flow are
121 zonally uniform but the correlations are explicitly local (model 1) and (ii) cases with in-phase
122 variability between remote longitudes (model 2). Second, the models make clear that the
123 spectra of variance yields insight into the role of dynamical annularity in driving the leading
124 EOF.

3. Theoretical Insight

For systems with statistical annularity, as in models X_1 and X_2 , the EOFs can be entirely characterized based on the covariance structure $f(\Delta\lambda)$. Batchelor (1953) solved the EOF problem for cases with zonally uniform statistics in his analysis of homogeneous, isotropic turbulence in a triply periodic domain. Our discussion is the 1-D limit of this more comprehensive analysis. If the statistics are zonally uniform (i.e., homogeneous), then EOF analysis will yield a pure Fourier decomposition of the flow. All EOFs will come in degenerate pairs expressing the same fraction of variance, except for the single wavenumber 0 (annular) mode¹.

The ordering of the Fourier coefficients depends on the Fourier decomposition of f . The covariance function $f(\Delta\lambda)$ is defined for $0 \leq \Delta\lambda \leq \pi$, where we express longitude in radians. The variance associated with a mode of wavenumber k is then given by

$$\text{var}(k) = \frac{1}{\pi} \int_0^\pi f(\lambda) \cos(k\lambda) d\lambda \quad (3)$$

For all k other than 0, there will be two modes, each characterizing this amount of variance.

Setting $k = 0$ in (3) shows that the integral of the autocorrelation function determines the strength of the annular mode. For systems with zonally uniform statistics, there is thus a nice interpretation of the strength of the annular mode: the fraction of the variance expressed by the annular mode is simply the “average” of the covariance function between a given base point and all other points. This will hold even in cases where the annular mode is not the first EOF.

Returning to the simple stochastic models in Section 2, we can now see how the two models were designed to have the same annular mode. The average value of the two covariance functions in Fig. 1c is 0.2 in both cases, so that the “annular mode” in each model explains

¹For a discrete system with n points in longitude, the missing partner to the wavenumber 0 mode is one of the wavenumber $n/2$ modes which is degenerate, appearing constant on the discrete grid. But for any realistic geophysical flow the variance decays quickly for high wavenumbers and this mode is insignificant.

147 20% of the total variance. In model X_1 , the average correlation of 0.2 derives solely from the
 148 strong positive correlation over half a hemisphere. That is, the annular mode is the most
 149 important EOF, but it only reflects the annularity of the statistics. In model X_2 , half of the
 150 variance associated with the annular mode can be attributed to dynamical annularity, as
 151 given by the global baseline correlation of 0.1. The other half is attributable to the positive
 152 correlation on local scales, reflecting the spatial redness of the circulation.

153 Model X_2 shows that even in a system with dynamical annularity, the “strength” of the
 154 annular model is enhanced by the spatial redness of the flow, which exists independent of
 155 underlying dynamical annularity. The weaker spatial redness of the flow in model X_2 relative
 156 to X_1 is visibly apparent in the structure of its samples (compare Fig. 1a and b), while the
 157 presence of coherent dynamical annularity leads to the large gap between the fraction of
 158 variance associated with wavenumber 0 and other waves in the EOF spectrum in Fig. 1c.
 159 It follows that an annular EOF is more likely to reflect dynamical annularity when there is
 160 large separation between the variance explained by it and higher order modes. In this case,
 161 the “average correlation” over all longitudes arises from far field correlation, *not just* the
 162 spatial redness of the circulation.

163 The models in Section 2 are two examples from a family of stochastic systems with spatial
 164 correlation structure

$$f(\lambda) = (1 - \beta)e^{-(\lambda/\alpha)^2} + \beta, \quad (4)$$

165 illustrated graphically in Fig. 3a. The parameter α is the spatial decorrelation scale (defined
 166 as the Gaussian width of the correlations in units of radians) and parameter β is the baseline
 167 annular correlation of the model. For systems with this spatial decorrelation structure, the
 168 leading EOF is always annular and the second and third EOFs always have wave 1 structure,
 169 even if there is no annular correlation (i.e., $\beta = 0$). This follows from the fact that a Fourier
 170 transform of a Gaussian is a Gaussian, such that power is always maximum at zero and
 171 decays with higher wavenumbers.

172 Fig. 3b summarize the variance explained by the leading EOFs of the system considered

173 in Fig. 3a as a function of the spatial decorrelation scale (ordinate) and the amplitude of
 174 the baseline annular correlation (abscissa). The contours indicate the variance explained
 175 by the leading (annular) EOF; the shading indicates the ratio of the variance between the
 176 leading and second (wavenumber one) EOFs. Dark blue shading indicates regions where
 177 the EOFs are degenerate (explain the same amount of variance). White shading indicates
 178 regions where the first EOF explains about twice the variance of the second EOF.

179 At the origin of the plot ($\alpha \rightarrow 0$ and $\beta = 0$), the system approaches the white noise limit,
 180 and all EOFs become degenerate. Traveling right along the x-axis from the origin (i.e.,
 181 keeping the spatial decorrelation scale α infinitesimally small and increasing the baseline
 182 annular correlation with β), we find that the variance associated with the wavenumber 0
 183 annular mode is simply given by the value of β . Here the spatial decorrelation scale collapses
 184 to a single longitude, so all higher modes are degenerate, and the strength of the annular
 185 mode derives entirely from dynamical annularity.

186 If one instead travels upward from the origin, allowing α to increase but keeping $\beta = 0$, the
 187 strength of the annular mode increases as well, despite their being no dynamical annularity.
 188 These are systems where the annular mode only reflects the *annularity of the statistics*, not
 189 *annularity of the motions*. As α gets increasingly large, positive correlations will develop
 190 at all longitudes by virtue of the fact that the spatial decorrelation scale is longer than a
 191 latitude circle. At this point, the spatial redness of the atmospheric motions gives rise to a
 192 baseline annular correlation due to the relatively short length of the latitude circle. When
 193 the spatial redness of the flow exceeds half of a latitude circle (0.5 on the ordinate axis),
 194 then the variance of the leading (annular) EOF explains \sim twice the variance of the second
 195 (wavenumber one) EOF.

196 Model 1 sits in the blue shaded region along the ordinate (see blue circle in Fig. 3b), with
 197 a spatial decorrelation scale of approximately 0.23 radians. Model 2 (the red square) was
 198 designed to have baseline annular correlation of 0.1 (i.e., $\beta = 0.1$), but with an annular mode
 199 that express the same fraction of variance, requiring a local correlation $\alpha \approx 0.13$ radians.

200 The simple models considered in this and the previous section provide insight into the
201 conditions that give rise to annular EOFs, and to the importance of the variance explained
202 by the leading EOFs in distinguishing between statistical and dynamical annularity. In the
203 following sections we apply these insights to output from a general circulation model and
204 observations. In the case of complex geophysical flows with out-of-phase correlations between
205 remote longitudes (i.e., teleconnections), one must consider not only the variance explained
206 by the leading EOFs, but also the spatial correlation structure $f(\Delta\lambda)$.

207 **4. The annularity of the circulation in models and re-** 208 **analysis**

209 How does the balance between dynamical vs. statistical annularity play out in general
210 circulation models and observations? In this section, we apply the insights gained from the
211 simple models to longitudinal variations of the atmospheric circulation at a single latitude,
212 e.g., variations in sea level pressure or geopotential height at 50°S. We focus on a single
213 latitude to provide a direct analogue to the simple one-dimensional stochastic models in
214 previous sections, albeit a single latitude serves as a stiff test for annular behavior. The
215 northern and southern annular mode patterns are based on EOF analysis of two-dimensional
216 SLP or geopotential height fields, where spherical geometry naturally connects the circulation
217 at all longitudes over the pole.

218 *a. Annular variability in a dry dynamical core*

219 We first consider a moisture free, 3-dimensional primitive equation model on the sphere,
220 often referred to as a dry dynamical core. The model is run with a flat, uniform lower
221 boundary, so that all the forcings are independent of longitude. Hence the circulation is
222 statistically annular, making it an ideal starting point to connect with the theory outlined

223 in the previous section.

224 The model is a spectral primitive equation model developed by the Geophysical Fluid Dy-
225 namics Laboratory (GFDL), run with triangular truncation 42 (T42) spectral resolution and
226 20 evenly spaced σ -levels in the vertical. It is forced with Held and Suarez (1994) “physics,”
227 a simple recipe for generating a realistic global circulation with minimal parameterization.
228 Briefly, all diabatic processes are replaced by Newtonian relaxation of the temperature to-
229 ward an analytic profile approximating an atmosphere in radiative-convective equilibrium,
230 and interaction with the surface is approximated by Rayleigh friction in the lower atmo-
231 sphere. The equilibrium temperature profile is independent of longitude and time, so there
232 is no annual cycle.

233 A key parameter setting the structure of the equilibrium temperature profile is the tem-
234 perature difference between the equator and pole, denoted $(\Delta T)_y$ by Held and Suarez (1994).
235 As explored in a number of studies (e.g., Gerber and Vallis 2007; Simpson et al. 2010;
236 Garfinkel et al. 2013), the strength of coupling between the zonal mean jet and baroclinic
237 eddies is sensitive to the meridional structure of the equilibrium temperature profile. A
238 weaker temperature gradient leads to stronger zonal coherence of the circulation and en-
239 hanced persistence of the annular mode. We use this sensitivity to contrast integrations
240 with varying degrees of dynamical annularity.

241 The temperature difference $(\Delta T)_y$ strongly influences the climatology of the model, as
242 illustrated by the near surface winds (blue curves) in Fig. 4, and can be compared with
243 similar results based on ERA-Interim reanalysis in Fig. 6. The results are based on 10,000
244 day integrations, exclusive of a 500 day spin up. The default setting for $(\Delta T)_y$ is 60° C, and
245 drives a fairly realistic equinoctial climatology with jets at 46° latitude in both hemispheres.
246 With a weaker temperature gradient, $(\Delta T)_y = 40^\circ$ C, the jets weaken and shifts equatorward
247 to approximately 38° .

248 The annular modes, defined as the first EOF of zonal mean SLP following Gerber et al.
249 (2008) and Baldwin and Thompson (2009), are illustrated by the red curves in in Fig. 4. By

250 definition, the positive phase of the model annular models is defined as low SLP over the
251 polar regions and thus a poleward shift of the model jet. The centers of action of the model
252 annular modes in sea level pressure vary between the two simulations, and are indicated by
253 the vertical black lines. In the following, we focus our analyses on latitudes corresponding
254 to the centers of action of the annular modes, contrasting it with similar analysis at their
255 nodes.

256 The top row in Fig. 5 compares the spatial decorrelation structure of sea level pressure
257 anomalies as a function of longitude at these three key latitudes. Results for the integration
258 with weak and standard HS temperature gradients are indicated by blue and red colors,
259 respectively. The bottom row shows the variances explained by the leading EOFs of SLP
260 calculated along the same latitude bands (i.e., the EOFs are calculated as a function of
261 longitude and time along the indicated latitude bands). We applied a 10 day low pass Lanczos
262 filter (Duchon 1979) to the data before our analysis to reduce the influence of synoptic
263 scale variability, but the results are qualitatively similar when based on daily or monthly
264 mean data. To further reduce the sampling uncertainty, the autocorrelation functions were
265 averaged over all longitudes and the EOF spectra were computed directly with equation
266 (3). This has the effect of imposing zonally symmetric statistics, which would be the case
267 with infinite sampling, and the results are virtually identical if we use the full fields for the
268 calculations.

269 We focus first on the equatorward center of action of the annular mode (left column).
270 The spatial decorrelation scale of SLP anomalies is approximately 60° longitude in both
271 integrations (Fig. 5a). The east-west structure of the correlations reflects the scale of syn-
272 optic disturbances and wave trains emanating in both directions. The similarities between
273 the spatial decorrelation scales reflects the fact that the deformation radius is similar in
274 both runs. The most striking difference between the two runs lies in their baseline annular
275 correlations. In the case of $(\Delta T)_y = 40$ the east-west structure of the correlations rides on
276 top of a zonally uniform correlation of approximately 0.3. In the case of the model with

277 $(\Delta T)_y = 60$, there is a weaker baseline correlation of approximately 0.1.

278 The difference in the underlying annularity of the flow explains the differences in the
279 variance spectra shown in Fig. 5d. In both model configurations, the leading EOFs are
280 annular; higher order modes generally increase monotonically in wavenumber with the ex-
281 ception of waves 5 and 6, which explain larger fractions of the variance than waves 3 and 4,
282 consistent with the synoptic structure of the correlation functions. The distinction between
283 the EOFs between the two model configurations lies in their variance spectra. In the case
284 of $(\Delta T)_y = 40$, the annular mode explains more than four times the variance of the second
285 EOF. In the case of $(\Delta T)_y = 60$, the annular mode explains about two times the variance
286 of the second EOF.

287 The differences in the variance spectra for the two model configurations are consistent
288 with the theoretical arguments outlined in the previous section. Both model configurations
289 exhibit dynamical annularity, as evidenced by the fact the spatial correlations are > 0 at all
290 longitudes. However, the dynamical annularity is much more pronounced for the $(\Delta T)_y = 40$
291 configuration, consistent with the larger ratio in variance explained between the first and
292 second EOFs. The $(\Delta T)_y = 60$ configuration is reminiscent of the simple stochastic model
293 X_2 , where the leading EOF explains approximately 20% of the variance in the flow: half due
294 to the dynamical annularity; half due to the spatial redness of the flow.

295 The annularity of flow is notably different along the node of the annular mode, which
296 coincides roughly with the maximum in the climatological jet stream (Fig. 5b and e). The
297 leading EOFs of SLP along the nodes of the annular modes are again annular, as is the
298 case at the equatorward centers of action (not shown). But along this latitude, there is no
299 apparent baseline annular correlation in either model configuration (Fig. 5b). Accordingly,
300 the EOF variance spectra exhibit little distinction between the variance explained by the
301 first and second EOFs. The enhanced dynamical annularity in the $(\Delta T)_y = 40$ case is thus
302 associated only with vacillations of the jet stream's position, not fluctuations in its strength,
303 which would be reflected by dynamical annularity in SLP at this latitude.

304 At the minimum of the annular mode pattern on the poleward flank of the jet stream,
305 Fig. 5c and f, the relatively small size of the latitude circle leads to a strong baseline annular
306 correlation and thus clear dominance of the annular mode in the variance spectra. The
307 spherical effect is more pronounced for the $(\Delta T)_y = 60$ case since the minimum in the
308 EOF pattern is located very close to the pole (Fig. 4). As the length of the latitude circle
309 approaches the scale of the deformation radius, a single synoptic scale disturbance connects
310 all longitudes, enforcing zonally uniform statistics. While the result appears trivial in this
311 light, this geometric effect may play a significant role in helping the annular mode rise above
312 other modes in two-dimensional EOF analysis. The flow is naturally zonally coherent near
313 the pole, and the tendency for anticorrelation between pressures at polar and middle latitudes
314 may play a role in generating annular-scale motions at lower latitudes (e.g., Ambaum et al.
315 2001; Gerber and Vallis 2005).

316 Its important to note that the circulation is more realistic with the default Held and
317 Suarez (1994) setting of $(\Delta T)_y = 60$, where the flow exhibits relatively modest zonal co-
318 herence. The stronger dynamical annularity in the $(\Delta T)_y = 40$ configuration is due to the
319 weak baroclinicity of the jet and the zonally uniform boundary conditions. When zonal
320 asymmetries are introduced to the model, the uniform motions are much reduced, even with
321 weak temperature forcing (Gerber and Vallis 2007). Zonal asymmetries on Earth will thus
322 likely both reduce the strength of globally coherent motions in the sense of equation (1), and
323 break the assumption of uniform statistics in the sense of equation (2). We find, however,
324 that both dynamical and statistical annularity are highly relevant to flow in reanalysis, at
325 least in the Southern Hemisphere.

326 *b. Annular variability in reanalysis*

327 The data used in this section are derived from the European Center for Medium Range
328 Weather Forecasting (ECMWF) Interim Reanalysis (ERA-I; Dee and coauthors 2011) over
329 the period 1979 to 2013. All results are based on anomalies, where the annual cycle is defined

330 as the long-term mean over the entire 35 year period. As done for the dynamical core, a 10
331 day low pass filter is applied to all data before computing correlations and performing the
332 EOF analyses. Note that qualitatively similar results are derived from daily and monthly-
333 mean data.

334 Fig. 6 shows the meridional structures of (i) the climatological zonal mean zonal wind at
335 850 hPa and (ii) the southern and northern annular modes. The annular mode time series
336 are defined as the standardized leading PCs of zonal mean 850 hPa geopotential height,
337 Z_{850} , between 20-90 degrees latitude. Since the time series are standardized, the regression
338 patterns shown in Fig. 6 reveal the characteristic amplitude of a one standard deviation
339 anomaly in the annular modes. While the long-term mean circulation differs considerably
340 between the two hemispheres, the annular modes are remarkably similar, although the NAM
341 is slightly weaker than the SAM, consistent with the weaker climatological jet. Gerber and
342 Vallis (2005) suggest that the meridional structure of the annular modes tend to be fairly
343 generic, constrained largely by the geometry of the sphere and the conservation of mass and
344 momentum.

345 The longitudinal correlation structures derived from the observations are not constrained
346 to be uniform with longitude, as is the case for the dry dynamical core. Nevertheless, they are
347 very similar from one base meridian to the next, particularly in the Southern Hemisphere.
348 For example, Fig. 7a shows four single point covariance maps based on Z_{850} at 50°S: the
349 covariance between Z_{850} at base points 0°, 90°E, 180°, and 90°W with all other longitudes.
350 We have shifted the four regression plots so that the base points overlies each other at the
351 center of the plot. Aside from slight variations in amplitude, there is remarkable uniformity
352 of the east-west correlation structure in the midlatitudes Southern Hemisphere circulation:
353 nearly all of the curves collapse upon each other. The correlation structures are positively
354 correlated over a range of approximately ± 60 degrees longitude and exhibit alternating
355 negative and positive lobes beyond that point. There is little evidence of global correlation,
356 as is the case with the default Held and Suarez (1994) model.

357 Fig. 7b extends the analysis in the top panel to include averages over all base meridians for
358 geopotential data at all latitudes. The figure is constructed as follows: (i) at a given latitude,
359 we calculate the zonal covariance structure for all possible base meridians, as opposed to just
360 four in Fig. 7a, (ii) we then average the resulting covariance structures after shifting them
361 to a common base meridian, (iii) we normalize the resulting “average covariance structure”
362 by the variance to convert to correlation coefficients, and lastly (iv) we repeat the analysis
363 for all latitudes. The resulting “average correlation structures” for 850 hPa geopotential
364 height are indicated by the shading in Fig. 7b. The black curve denotes the zero contour;
365 the gray curves denote a distance of ± 2500 km from the base longitude to provide a sense
366 of the sphericity of the Earth. Normalizing the covariance functions by the variance allows
367 us to compare the longitudinal structures in the tropics and the midlatitudes on the same
368 figure; otherwise the increase in the variance of Z_{850} with latitude (illustrated in Fig. 7c)
369 yields much larger amplitudes in the extratropics.

370 At middle latitudes, positive correlations extend over a distance of approximately 2500
371 km outward from the base longitude. Towards the polar regions, the autocorrelations extend
372 over much of the latitude circle due to the increasingly smaller size of the zonal ring. The
373 austral polar regions are exceptional, in that the correlations extend not only around the
374 circumference of the latitude circle, but also well beyond 2500 km as far equatorward as
375 60°S . Interestingly, tropical geopotential height is also correlated over long distances. The
376 significant positive correlations at tropical latitudes are robust at most individual longitudes
377 outside of the primary centers of action of ENSO (not shown). The in-phase behavior
378 in tropical geopotential height is consistent with the dynamic constraint of weak pressure
379 gradients at tropical latitudes (Charney 1963; Sobel et al. 2001) and will be investigated
380 further in future work. Note that the amplitude of variations in geopotential height are
381 more than an order of magnitude weaker in the tropics than midlatitudes, as illustrated in
382 Fig. 7c.

383 The results shown in Fig. 7 are based on 10 day low pass filtered data. As discussed in

384 Wettstein and Wallace (2010), large-scale structures in the atmospheric circulation are in-
385 creasingly prevalent at lower frequency timescales. Analogous calculations based on monthly
386 mean data (not shown) reveal a slight extension of the region of positive correlations at all
387 latitudes, but overall the results are qualitatively unchanged. Notably, the midlatitude cor-
388 relation structure is still dominated by alternating negative and positive anomalies beyond
389 2500 km, with little evidence of zonally coherent motions.

390 How does the average correlation structure shown in Fig. 7b project onto the EOFs of
391 the circulation? Fig. 8 characterizes the (top) “predicted” and (bottom) “actual” EOFs of
392 zonally-varying Z_{850} calculated separately for each latitude (e.g., results at 60° N indicate the
393 variance expressed by EOFs of Z_{850} sampled along the 60° N latitude circle). The “predicted”
394 EOFs are found assuming the statistics of Z_{850} are zonally uniform. In this case, the results
395 of the EOF analysis correspond to a Fourier decomposition of the flow (see discussion in
396 Section 3), and the variance captured by each wavenumber is determined by the average
397 correlation structure (Fig. 7b) applied to (3). Wavenumber 0 (i.e., annular mode) variability
398 emerges as the leading predicted EOF of the flow at virtually all latitudes, but explains a
399 much larger fraction of the variance of the flow in the tropics and polar regions than it does
400 in middle latitudes, where wavenumbers 0, 1, 2, and 3 are of nearly equal importance. The
401 weak amplitude of wavenumber 0 variability in middle latitudes is consistent with the lack
402 of zonally coherent motions in the average correlation structures shown in Fig. 7b.

403 The “actual” EOFs are computed directly from Z_{850} , and thus do not assume that the
404 statistics of the flow are zonally uniform. Red dots indicate when the EOF is dominated
405 by wavenumber 0 variability, orange dots by wave 1 variability, and so forth for higher
406 wavenumbers. (Note that for the predicted EOFs, all wavenumbers other than 0 include two
407 modes in quadrature that account for equal variance, whereas for the actual EOFs, the two
408 modes associated with each wavenumber are not constrained to explain the same fraction of
409 the variance.) Comparing the top and bottom panels, it is clear that the EOFs predicted
410 from the average correlation structure, assuming zonally-uniform statistics, provide useful

411 insight into the true EOFs of the flow. The meridional structures of the variance explained
412 by the leading predicted and actual EOFs are very similar: in the high latitudes and tropics,
413 the first mode is dominated by wavenumber 0 variability and explains a much larger fraction
414 of the flow than EOF2; in the midlatitudes, the EOFs cluster together and are largely
415 degenerate.

416 The key point derived from Figs. 7 and 8 is that the “average correlation function” pro-
417 vides a clear sense of where the EOFs of the flow derive from robust dynamical annularity.
418 The circulation exhibits globally coherent motions in the tropics and high latitudes, partic-
419 ularly in the SH high latitudes (Fig. 7), and it is over these regions that the leading EOFs
420 predicted from the average correlation function (Fig. 8a) and from actual variations in the
421 flow (Fig. 8b) exhibit robust wavenumber 0 variability. In contrast, the circulation does
422 not exhibit globally coherent variations at middle latitudes (Fig. 7b), and thus both the
423 predicted and actual EOFs of the flow are degenerate there (Fig. 8). *Annular variations in*
424 *lower tropospheric geopotential height are consistent with dynamical annularity of the flow*
425 *in the polar and tropical regions, but statistical annularity at middle latitudes.*

426 Fig. 9 explores the average correlation structure in three additional fields. Fig. 9a,b show
427 results based on the zonal wind at 850 hPa (U_{850}), which samples the barotropic component
428 of the circulation, and thus emphasizes the eddy-driven jet in middle latitudes. Fig. 9c,d are
429 based on the zonal wind at 50 hPa and (U_{50}), which samples both the QBO and variations in
430 the stratospheric polar vortices, and Fig. 9e,f, the eddy kinetic energy at 300 hPa (EKE_{300}),
431 which samples the baroclinic annular mode (Thompson and Barnes 2014).

432 The most pronounced zonal correlations in U_{850} are found in two locations: (i) along
433 60 degrees South, where positive correlations wrap around the latitude circle, and (ii) in
434 the deep tropics, where positive correlations extend well beyond the 2500 km isopleths. At
435 ~ 60 degrees South, the zonally coherent variations in the zonal flow follow from geostrophic
436 balance and the coherence of the geopotential height field over Antarctica, as observed in
437 Fig. 7b. In the subtropics, the far reaching correlations follow from geostrophic balance

438 and the coherence of the geopotential height field in the tropics. At the equator, where
439 geostrophic balance does not hold, Z_{850} exhibits globally coherent motions (consistent with
440 weak temperature gradients in the tropics), while U_{850} becomes significantly anticorrelated
441 at a distance. As a result, a zonally uniform annular mode dominates the EOF spectrum
442 of Z_{850} in the tropics (Fig. 8b) whereas wavenumber 1 tends to dominate latitudinal EOF
443 analysis of U_{850} (not shown). Neither Z_{850} (Fig. 7b) or U_{850} (Fig. 9a) exhibit zonally coherent
444 motions at midlatitudes, where the autocorrelation function decays to zero ~ 2500 kilometers
445 and oscillates in the far field.

446 The results shown in Figs. 7b and 9a are representative of the correlation structure of
447 geopotential height and zonal wind throughout the depth of the troposphere (e.g., very
448 similar results are derived at 300 hPa; not shown). However, the correlation structure of the
449 zonal flow changes notably above the tropopause, as indicated in Fig. 9c and d. Consistent
450 with the increase in the deformation radius in the stratosphere, the scale of motions increases
451 (note that the grey lines now indicate the $\pm 5,000$ km isopleths). The most notable differences
452 between the troposphere and stratosphere are found in the tropics, where the Quasi Biennial
453 Oscillation (QBO) leads to an overwhelming annular signal. Marked annularity is also found
454 in the high latitudes, in the vicinity of both extratropical polar vortices. As observed in the
455 analysis of the tropospheric zonal wind and geopotential height, however, there is no evidence
456 of dynamical annularity in the midlatitudes.

457 The average correlation structure of EKE_{300} (Fig. 9e) is notably different. Unlike Z or
458 U , the zonal correlation of EKE is remarkably similar across all latitudes, with a slight
459 peak in the physical scale of the correlation in the Southern Hemisphere midlatitudes where
460 the baroclinic annular mode has largest amplitude (e.g., Thompson and Woodworth 2014).
461 Interestingly, EKE_{300} remains positively correlated around the globe at all latitudes, albeit
462 very weakly in the far field. The non-negative decorrelation structure leads to the dominance
463 of a zonally uniform “annular mode” in EKE at each individual latitude poleward of 25°S ,
464 as shown in Fig. 10. However, the separation between the first and second modes (which

465 characterize wavenumber 1 motions) is modest at most latitudes. The largest separations
466 between the first and second EOFs EKE_{300} are found near 45° , where the top annular EOF
467 represents about 16% of the variance, compared to about 11% for the second and third
468 EOFs.

469 *c. Quantifying the role of dynamical annularity in EKE_{300} with the stochastic model*

470 At first glance, the weak separation between the first and second EOFs of EKE_{300}
471 suggests that much of the annular signal owes itself to local correlations, i.e., statistical
472 annularity. However, a comparison of the EOFs of the observations with those derived
473 from the “Gaussian + baseline” model explored in Sections 2 and 3 allows us to be more
474 quantitative about the relative role of dynamical vs. statistical annularity in the context of
475 the baroclinic annular mode.

476 Fig. 11 compares (a) the zonal correlation structure and (b) EOF spectrum of the 300
477 hPa eddy kinetic energy at 46°S with three fits of the simple stochastic model, each designed
478 to capture key features of the observed behavior. Recall that the model has two parameters:
479 the width of local correlation, α , and the baseline correlation strength, β . As our goal is to
480 focus on the relative role of dynamical annularity, characterized by the difference between
481 the variance expressed by the top EOF (annular mode) and higher order modes, we remove
482 one degree of freedom by requiring that the top EOF express the same fraction of variance in
483 both the simple model and the reanalysis. Hence the first mode explains 16% of the variance
484 for all cases in Fig. 11b. From equation (3), this condition is equivalent to keeping the total
485 integral of the correlation structure fixed.

486 In the first fit (red curve, Fig. 11a), we optimize the stochastic model at short range,
487 approximating the fall in local correlation in EKE as a Gaussian with width $\alpha = 17$ degrees.
488 To maintain the variance expressed by the top EOF, parameter β must then be set to 0.08.
489 This choice effectively lumps the midrange shoulder of the EKE_{300} correlation ($30\text{-}100^\circ$)
490 with the long range ($100\text{-}180^\circ$), where the observed correlation drops to about 0.03. As

491 a result, the stochastic model exhibits a stronger separation between the first and second
 492 EOFs than for EKE_{300} (red triangles vs. black squares in Fig. 11b).

493 An advantage of fitting the data to the simple stochastic model is that it allows us to
 494 explicitly quantify the role of dynamical annularity. Since the variance expressed by the
 495 annular mode is just the integral of correlation function (equation 3), the contribution of the
 496 long range correlation (dynamical annularity) to the total power of the annular mode is:

$$\frac{\int_0^{180} \beta d\lambda}{\int_0^{180} [(1 - \beta)e^{-(\lambda/\alpha)^2} + \beta] d\lambda} \approx \frac{\beta}{\frac{\alpha(1-\beta)\sqrt{\pi}}{360} + \beta} \quad (5)$$

497 where we have expressed longitude λ and parameter α in degrees. For the approximation
 498 on the left hand side, we assume that $\alpha \ll 180$, such that the local correlation does not
 499 significantly wrap around the latitude circle. For the “red” model in Fig. 11, dynamical
 500 annularity accounts for half of the total strength of the annular mode. Given the fact that it
 501 exhibits a stronger separation between the first and second EOFs, however, this is an upper
 502 bound on the role of dynamical annularity in EKE_{300} at 46°S.

503 We obtain a lower bound on the dynamical annularity with the blue fit in Fig. 11a, where
 504 the correlation structure is explicitly matched at long range. To conserve the total integral,
 505 parameter α in this case must be set to 27°, effectively lumping in the shoulder between
 506 30 and 100° with the local correlation. These parameters would suggest that dynamical
 507 annularity contributes only 1/5th of annular mode variance. This is clearly a lower limit,
 508 however, as the separation between the first and second EOFs (Fig. 11b) is too small relative
 509 to that of EKE_{300} .

510 Lastly, we use both degrees of freedom of the stochastic model to find an optimal fit of
 511 the EOF spectrum, matching the variance expressed by the top two EOFs (effectively the
 512 top three, as higher order modes come in pairs). The fit, with parameters $\alpha = 23^\circ$ and
 513 $\beta = 0.05$, is not shown in Fig. 11a (to avoid clutter), but the resulting EOF spectrum is
 514 illustrated by the green triangles in Fig. 11b. With this configuration, dynamical annularity
 515 contributes approximately 1/3rd of the annular mode, leaving the remaining two thirds to
 516 statistical annularity associated with the local redness of the EKE. The EOF spectra of this

517 model diverges from EKE_{300} for higher order modes, such that we should take this as a
518 rough estimate of the true role of dynamical annularity in the Baroclinic Annular Mode.

519 The location of the three models (lower, optimal, and upper bounds), are marked by the
520 black x's in Fig. 3b, to put them in context of earlier results. The fits roughly fill in the
521 space between models X_1 and X_2 , but on a lower contour where the annular mode expresses
522 16% of the total variance, as opposed to 20%. The rapid increase in the role of dynamical
523 annularity (from 1/5 to 1/2) matches the rapid ascent in the importance of EOF 1 relative
524 to EOF 2, emphasizing the utility of this ratio as an indicator of dynamical annularity.

525 5. Concluding Remarks

526 We have explored the conditions that give rise to annular patterns in Empirical Orthog-
527 onal Function analysis across a hierarchy of systems: highly simplified stochastic models,
528 idealized atmospheric GCMs, and reanalyses of the atmosphere. Annular EOFs can arise
529 from two conditions, which we term *dynamical annularity* and *statistical annularity*. The
530 former arises from zonally coherent dynamical motions across all longitudes, while the latter
531 arises from zonally coherent statistics of the flow (e.g., the variance), even in the absence of
532 significant far field correlations. Atmospheric reanalyses indicate that both play important
533 roles in the climate system and may aid in the interpretation of climate variability, but only
534 dynamical annularity reflects zonally coherent motions in the circulation.

535 In general, dynamical annularity arises when the dynamical scales of motion approach
536 the scale of the latitude circle. The average zonal correlation structure (e.g., Fig. 7) thus
537 provides a robust measure of dynamical annularity. In addition, the simple stochastic model
538 suggests that the degree of dynamical annularity in a leading EOF is indicated by the ratio
539 of the variances explained by the first two zonal EOFs of the flow. As a rule of thumb, if
540 the leading annular EOF explains more than twice the variance of the second EOF, then
541 dynamical annularity plays a substantial role in the annular mode. Note, however, that this

542 intuition does not necessarily apply to two-dimensional EOFs in latitude-longitude space,
543 where coherence of meridional variability can lead to dominance of an annular EOF, even
544 when there is explicitly no dynamical annularity (e.g., Gerber and Vallis 2005).

545 Annular EOFs always – at least partially – reflect statistical annularity of the circulation;
546 zonally coherent motions necessarily imply some degree of zonal coherence. Far field correla-
547 tion in the average zonal correlation structure robustly indicates dynamical annularity, but
548 quantification of the statistical annularity requires further analysis, either comparison of the
549 zonal correlation at different base points (e.g., Fig. 7a) or comparison of the predicted and
550 observed zonal EOFs (e.g., Figs. 8 and 10). The localization of the North Pacific and North
551 Atlantic storm tracks limits the utility of the zonal correlation structure in the Northern
552 Hemisphere troposphere. But the Southern Hemisphere tropospheric circulation is remark-
553 ably statistically annular, such that one can predict the full EOF spectrum from the average
554 correlation structure alone.

555 As discussed in Deser (2000) and Ambaum et al. (2001), the observed geopotential height
556 field does not exhibit robust far field correlations beyond ~ 60 degrees longitude in the
557 midlatitudes. However, the geometry of the sphere naturally favors a high degree of zonal
558 coherence at higher latitudes. Hence, the northern and southern annular modes do not
559 arise from dynamical annularity in the middle latitude tropospheric circulation, but derive
560 a measure of dynamical annularity from the coherence of their polar centers of action in
561 the geopotential height field. The dynamical annularity of the annular mode extends to the
562 zonal wind field at high latitudes in the Southern Hemisphere, but less so in the Northern
563 Hemisphere. Other regions where dynamical annularity plays a seemingly important role in
564 the circulation include:

- 565 i. the tropical geopotential height field, presumably because temperature gradients must
566 be weak in this region (e.g., Charney 1963),
- 567 ii. the tropospheric zonal flow near ~ 15 degrees latitude; these features arises via geostro-
568 phy and the dynamic annularity of the tropical Z field.

569 iii. the zonal wind field in the equatorial stratosphere, which reflects the QBO,
570 iv. the eddy kinetic energy in the midlatitude Southern Hemisphere, consistent with the
571 baroclinic annular mode and the downstream development of wave packets in the
572 austral stormtrack (Thompson et al. submitted). The dynamical annularity of the
573 eddy activity is surprising given the lack of dynamic annularity in the midlatitude
574 barotropic jets, which are intimately connected with the eddies through the baroclinic
575 lifecycle.

576 The annular leading EOFs of the midlatitude flow have been examined extensively in
577 previous work, but to our knowledge, the annular nature of tropical tropospheric Z has
578 received less attention. We intend to investigate this feature in more detail in a future study.

579 *Acknowledgments.*

580 EPG acknowledges support from the National Science Foundation through grant AGS-
581 1546585.

582

583

584 Technical details of the stochastic models

585 The stochastic models in Section 2 are, in a sense, constructed in reverse, starting with
 586 the desired result. We begin with the correlation structure f , as shown in Fig. 1c, and
 587 project it onto cosine modes as in (3). This gives us the EOF spectra shown in Fig. 2c,
 588 i.e., how much variance (which we now denote v_k) should be associated with each mode of
 589 wavenumber k . Note that not all correlation structures are possible. A sufficient criteria,
 590 however, is that the projection of every cosine mode onto f is non-negative (i.e., all $v_k \geq 0$).

591 Realizations of the models, as shown in 1a and b, are constructed by moving back into
 592 grid space,

$$X(\lambda, j) = v_k^{1/2} \delta_{0,j} + \sum_{k=1}^{\infty} (2v_k)^{1/2} [\delta_{k1,j} \sin(k\lambda) + \delta_{k2,j} \cos(k\lambda)]. \quad (\text{A1})$$

593 where all the $\delta_{k,j}$ are independent samples from a Normal distribution with unit variance
 594 and λ is given in radians. In practise only the top 15 wavenumbers are needed, as the
 595 contribution of higher order modes becomes trivial.

596 Note that it is possible to construct an infinite number of stochastic systems which
 597 have the same correlation structure f . We have take a simple approach by using the Normal
 598 distribution to introduce randomness. Any distribution with mean zero could be used, which
 599 would impact the variations in individual samples – and so the convergence of the system in
 600 j – but not the statistical properties in the limit of infinite sampling.

601

602

REFERENCES

603 Ambaum, M. H. P., B. J. Hoskins, and D. B. Stephenson, 2001: Arctic Oscillation or North
604 Atlantic Oscillation? *J. Climate*, **14**, 3495–3507.

605 Baldwin, M. P. and D. W. J. Thompson, 2009: A critical comparison of stratosphere-
606 troposphere coupling indices. *Quart. J. Roy. Meteor. Soc.*, **135**, 1661–1672.

607 Batchelor, G. K., 1953: *The Theory of Homogeneous Turbulence*. Cambridge University
608 Press, 197 pp.

609 Charney, J. G., 1963: A note on large-scale motions in the tropics. *J. Atmos. Sci.*, **20**,
610 607–609.

611 Dee, D. P. and . coauthors, 2011: The ERA-Interim reanalysis: configuration and per-
612 formance of the data assimilation system. *Quart. J. Roy. Meteor. Soc.*, **137**, 553–597,
613 doi:10.1002/qj.828.

614 Deser, C., 2000: On the teleconnectivity of the "arctic oscillation". *Geophysical Research*
615 *Letters*, **27 (6)**, 779–782, doi:10.1029/1999GL010945.

616 Dommenges, D. and M. Latif, 2002: A cautionary note on the interpretation of EOFs. *J.*
617 *Climate*, **15**, 216–225.

618 Duchon, C. E., 1979: Lanczos filtering in one and two dimensions. *J. Applied Meteor.*, **18**,
619 1016–1022.

620 Garfinkel, C. I., D. W. Waugh, and E. P. Gerber, 2013: The effect of tropospheric jet latitude
621 on coupling between the stratospheric polar vortex and the troposphere. *J. Climate*, **26**,
622 2077–2095, doi:10.1175/JCLI-D-12-00301.1.

- 623 Gerber, E. P. and G. K. Vallis, 2005: A stochastic model for the spatial structure of annular
624 patterns of variability and the NAO. *J. Climate*, **18**, 2102–2118.
- 625 Gerber, E. P. and G. K. Vallis, 2007: Eddy-zonal flow interactions and the persistence of
626 the zonal index. *J. Atmos. Sci.*, **64**, 3296–3311.
- 627 Gerber, E. P., S. Voronin, and L. M. Polvani, 2008: Testing the annular mode autocorrelation
628 timescale in simple atmospheric general circulation models. *Mon. Wea. Rev.*, **136**, 1523–
629 1536.
- 630 Hartmann, D. L. and F. Lo, 1998: Wave-driven zonal flow vacillation in the Southern Hemi-
631 sphere. *J. Atmos. Sci.*, **55**, 1303–1315.
- 632 Held, I. M. and M. J. Suarez, 1994: A proposal for the intercomparison of the dynamical
633 cores of atmospheric general circulation models. *Bull. Am. Meteor. Soc.*, **75**, 1825–1830.
- 634 Karoly, D. J., 1990: The role of transient eddies in low-frequency zonal variations of the
635 southern hemisphere circulation. *Tellus A*, **42**, 41–50, doi:10.1034/j.1600-0870.1990.00005.
636 x.
- 637 Kidson, J. W., 1988: Interannual variations in the Southern Hemisphere circulation. *J.*
638 *Climate*, **1**, 1177–1198.
- 639 Kutzbach, J. E., 1970: Large-scale features of monthly mean Northern Hemisphere anomaly
640 maps of sea-level pressure. *Mon. Wea. Rev.*, **98**, 708–716.
- 641 Lee, S. and S. B. Feldstein, 1996: Mechanism of zonal index evolution in a two-layer model.
642 *J. Atmos. Sci.*, **53**, 2232–2246.
- 643 Lorenz, D. J. and D. L. Hartmann, 2001: Eddy-zonal flow feedback in the Southern Hemi-
644 sphere. *J. Atmos. Sci.*, **58**, 3312–3327.
- 645 Lorenz, E. N., 1951: Seasonal and irregular variations of the Northern Hemisphere sea-level
646 pressure profile. *J. Meteor.*, **8**, 52–59.

647 Marshall, J., D. Ferreira, J.-M. Campin, and D. Enderton, 2007: Mean climate and vari-
648 ability of the atmosphere and ocean on an aquaplanet. *J. Atmos. Sci.*, **64**, 4270–4286,
649 doi:10.1175/2007JAS2226.1.

650 Robinson, W. A., 1991: The dynamics of low-frequency variability in a simple model of the
651 global atmosphere. *J. Atmos. Sci.*, **48**, 429–441.

652 Shindell, D. T., R. L. Miller, G. A. Schmidt, and L. Pandolfo, 1999: Simulation of recent
653 northern winter climate trends by greenhouse-gas forcing. *Nature*, **399**, 452–455.

654 Simpson, I. R., M. Blackburn, J. D. Haigh, and S. N. Sparrow, 2010: The impact of the
655 state of the troposphere on the response to stratospheric heating in a simplified GCM. *J.*
656 *Climate*, **23**, 6166–6185.

657 Sobel, A. H., J. Nilsson, and L. M. Polvani, 2001: The weak temperature gradient approxi-
658 mation and balanced tropical moisture waves. *J. Atmos. Sci.*, **58**, 3650–3665.

659 Thompson, D. W. J. and E. A. Barnes, 2014: Periodic variability in the large-scale Southern
660 Hemisphere atmospheric circulation. *Science*, **343**, 641–645, doi:10.1126/science.1247660.

661 Thompson, D. W. J., B. R. Crow, and E. A. Barnes, submitted: Intraseasonal periodicity
662 in the southern hemisphere circulation on regional spatial scales. *J. Atmos. Sci.*

663 Thompson, D. W. J. and J. M. Wallace, 1998: The Arctic Oscillation signature in the
664 wintertime geopotential height and temperature fields. *Geophys. Res. Lett.*, **25**, 1297–
665 1300.

666 Thompson, D. W. J. and J. M. Wallace, 2000: Annular modes in the extratropical circulation.
667 Part I: Month-to-month variability. *J. Climate*, **13**, 1000–1016.

668 Thompson, D. W. J. and J. D. Woodworth, 2014: Barotropic and baroclinic annular
669 variability in the Southern Hemisphere. *J. Atmos. Sci.*, **71**, 1480–1493, doi:10.1175/
670 JAS-D-13-0185.1.

- 671 Trenberth, K. E. and D. A. Paolino, 1981: Characteristic patterns of variability of sea level
672 pressure in the Northern Hemisphere. *Mon. Wea. Rev.*, **109**, 1169–1189.
- 673 Wallace, J. M. and D. S. Gutzler, 1981: Teleconnections in the geopotential height field
674 during the Northern Hemisphere winter. *Mon. Wea. Rev.*, **109**, 784–812.
- 675 Wallace, J. M. and D. W. J. Thompson, 2002: The Pacific center of action of the Northern
676 Hemisphere annular mode: Real or artifact? *J. Climate*, **15**, 1987–1991.
- 677 Wettstein, J. J. and J. M. Wallace, 2010: Observed patterns of month-to-month storm-track
678 variability and their relationship to the background flow. *J. Atmos. Sci.*, **67**, 1420–1437,
679 doi:10.1175/2009JAS3194.1.
- 680 Yu, J. Y. and D. L. Hartmann, 1993: Zonal flow vacillation and eddy forcing in a simple
681 GCM of the atmosphere. *J. Atmos. Sci.*, **50**, 3244–3259.

682 List of Figures

- 683 1 Two stochastic models of variability in longitude. (a) and (b) illustrate sample
684 profiles from models X_1 and X_2 , respectively. The y-axes are unitless, as each
685 model has been designed to have unit variance. (c) shows $\text{cov}_X(0, \lambda)$ for
686 each model, the covariance between variability at each longitude with that at
687 $\lambda = 0$. As the statistics are annular, the covariance structure can be fully
688 characterized by this one sample, i.e., $\text{cov}_X(\lambda_1, \lambda_2) = \text{cov}_X(0, |\lambda_1 - \lambda_2|)$. 33
- 689 2 The EOF structure of the two stochastic models. (a) and (b) show the top
690 three EOFs for models 1 and 2, respectively, normalized to have unit variance.
691 In the limit of infinite sampling, the EOF patterns from the two models are
692 identical. (c) The models' EOF spectra, marking the fraction of the total
693 variance associated with each of the top 20 EOFs. 34
- 694 3 The impact of local vs. annular correlation in the “Gaussian + baseline”
695 family of stochastic models. (a) illustrates the parameters α and β which
696 characterize the correlation function $f(\lambda)$ for each model. (b) maps out the
697 variance expressed by the first EOF (black contours) and the ratio of the
698 variance expressed by the first EOF to that of the second (color shading) as a
699 function of α and β . The first EOF is always annular, and the second always a
700 wavenumber 1 pattern. The blue and red markers show the location of models
701 X_1 and X_2 (illustrated in Figs. 1 and 2) in parameter space, respectively; both
702 fall along the same black contour, as their top EOF expresses 0.2 of the total
703 variance. The black x's will be discussed in the context of Fig. 11 35

- 704 4 The mean jet structure and annular modes of the Held and Suarez (1994)
705 model for the (a) $(\Delta T)_y = 40$ and (b) $(\Delta T)_y = 60^\circ\text{C}$ integrations. The jet is
706 characterized by the time mean 850 hPa winds (blue lines, corresponding with
707 the left y-axes), and the annular mode is the first EOF of daily, zonal mean
708 SLP (red, right y-axes), normalized to indicate the strength of 1 standard
709 deviation anomalies. The latitudes of the node, equatorward and poleward
710 lobes of the annular mode are highlighted, and correspond with the analysis
711 in Fig. 5. 36
- 712 5 Characterizing the zonal structure of 10 day pass filtered SLP anomalies in
713 the Held and Suarez (1994) model. (a,d) and (c,f) show analysis based at
714 the latitude of the equatorward and poleward centers of action of the annular
715 mode, respectively, while (b,e) show analysis based at the nodes of the annular
716 mode. (a,b,c) show the zonal correlation structure $f(\lambda)$ and (d,e,f) the fraction
717 of variance associated with each of the top 20 EOFs for the integrations with
718 (blue) $(\Delta T)_y = 40$ and (red) $(\Delta T)_y = 60^\circ\text{C}$. 37
- 719 6 The same as Fig. 4, but for the (a) Southern and (b) Northern Hemispheres
720 in ECWMF Interim reanalysis, based on the period 1979-2013. To avoid
721 interpolation over mountainous regions, the annular modes are defined in
722 terms of daily, zonal mean 850 hPa geopotential height, Z_{850} , instead of SLP. 38

723 7 Characterizing the longitudinal correlation structure of 10 day low pass filtered
724 850 hPa geopotential height in ERA-Interim. (a) Sample single point corre-
725 lation maps at 46°S (the equatorward center of action of the SAM), shifted
726 so that base points line up. The black line is the mean of the four curves,
727 an “average single point correlation map”. (b) The average zonal correlation
728 structure of 10 day low pass filtered Z_{850} as a function of latitude. The con-
729 tour interval is 0.05, with black contours marking zero correlation, and gray
730 lines indicate a separation of 5000 km, to provide a sense of geometry on the
731 sphere. (c) The root mean square amplitude of 10 day low pass filtered Z_{850}
732 anomalies. 39

733 8 A comparison of predictions based on zonally uniform statistics to the actual
734 zonal EOF structure of 10 day low pass filtered Z_{850} . (a) For each latitude,
735 the fraction of variance associated with wavenumbers 0 to 6, given the average
736 zonal correlation structure in Fig. 7b and assuming zonally uniform statistics
737 (see text for details). (b) Again for each latitude, the fraction of variance
738 associated with the top five 1-D longitudinal EOFs, but now based on the full
739 flow. Large (small) colored dots indicate when a given wavenumber dominates
740 more than 75% (50%) of the power in the EOF, the color identifying the
741 respective wavenumber with the color convention in (a), i.e., red=wave 0,
742 orange=wave 1. 40

743 9 The average correlation structure of (a) zonal wind at 850 hPa, (c) zonal wind
744 at 50 hPa, and (e) eddy kinetic energy at 300 hPa. As in Fig. 7b, thin black
745 contours mark zero correlation and the thick gray contours give a sense of
746 sphericity, marking a separation of 5000 km as a function of latitude in (a)
747 and (e) and a distance of 10000 km in (c). Panels (b), (d), and (f) show
748 the root mean square amplitude of variations as a function latitude for each
749 variable, respectively. 41

- 750 10 The same as in Fig. 8b, but for eddy kinetic energy at 300 hPa. Zonal asym-
751 metry in the statistics lead to substantial mixing between wavenumbers in
752 the Northern Hemisphere (outside the polar cap) and tropics, such no sin-
753 gle wavenumber dominates each EOF. Statistical annularity in the Southern
754 Hemisphere, however, leads to a clearly order spectrum poleward of 25°S,
755 dominated by an annular (wavenumber 1) mode at all latitudes. 42
- 756 11 (a) Comparison between the average longitudinal correlation structure of
757 EKE_{300} at 46°S and two possible fits with the Gaussian + baseline model
758 of Section 3. As detailed in the text, the first fit (red) is optimized to cap-
759 ture the initial decay in correlation, while the second fit (blue) is optimized
760 for the long range correlation baseline. (b) The 1-dimensional EOF spectra
761 of EKE_{300} at 46°S, compared against the spectrum for the two fits of the
762 Gaussian + baseline model shown in (a), and a third model with parameters
763 $\alpha = 23^\circ$ and $\beta = 0.05$, as discussed in the text. 43

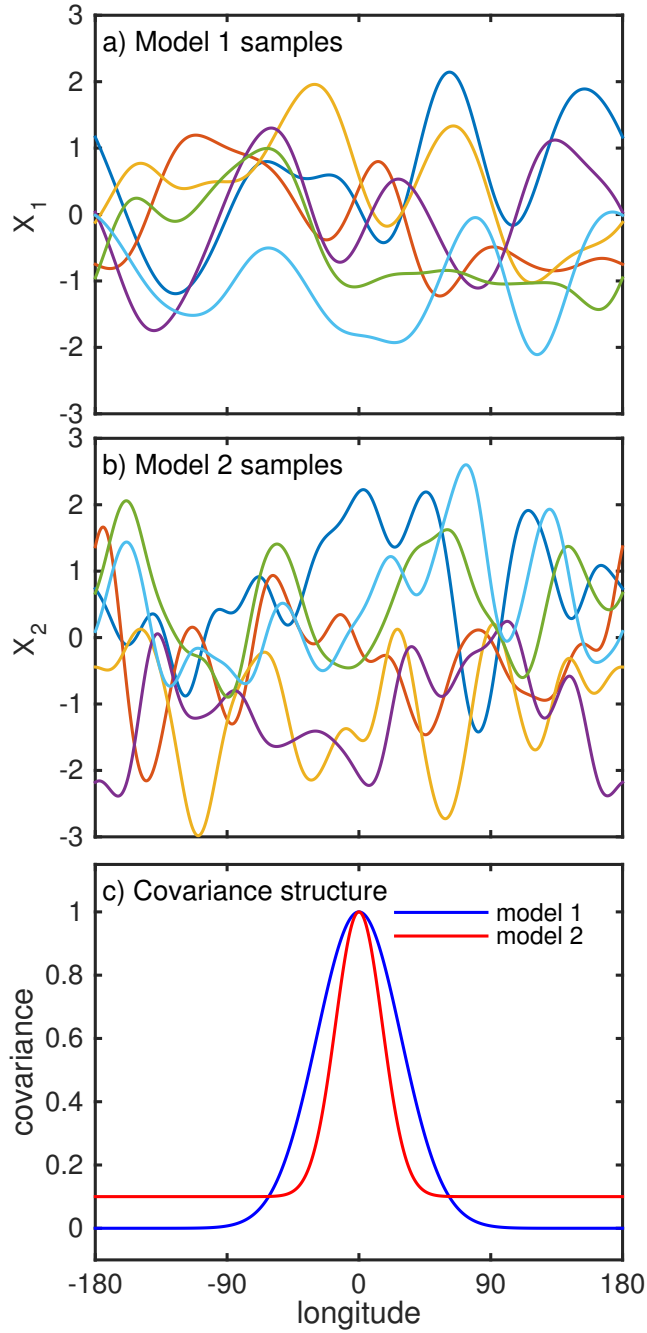


FIG. 1. Two stochastic models of variability in longitude. (a) and (b) illustrate sample profiles from models X_1 and X_2 , respectively. The y-axes are unitless, as each model has been designed to have unit variance. (c) shows $\text{cov}_X(0, \lambda)$ for each model, the covariance between variability at each longitude with that at $\lambda = 0$. As the statistics are annular, the covariance structure can be fully characterized by this one sample, i.e., $\text{cov}_X(\lambda_1, \lambda_2) = \text{cov}_X(0, |\lambda_1 - \lambda_2|)$.

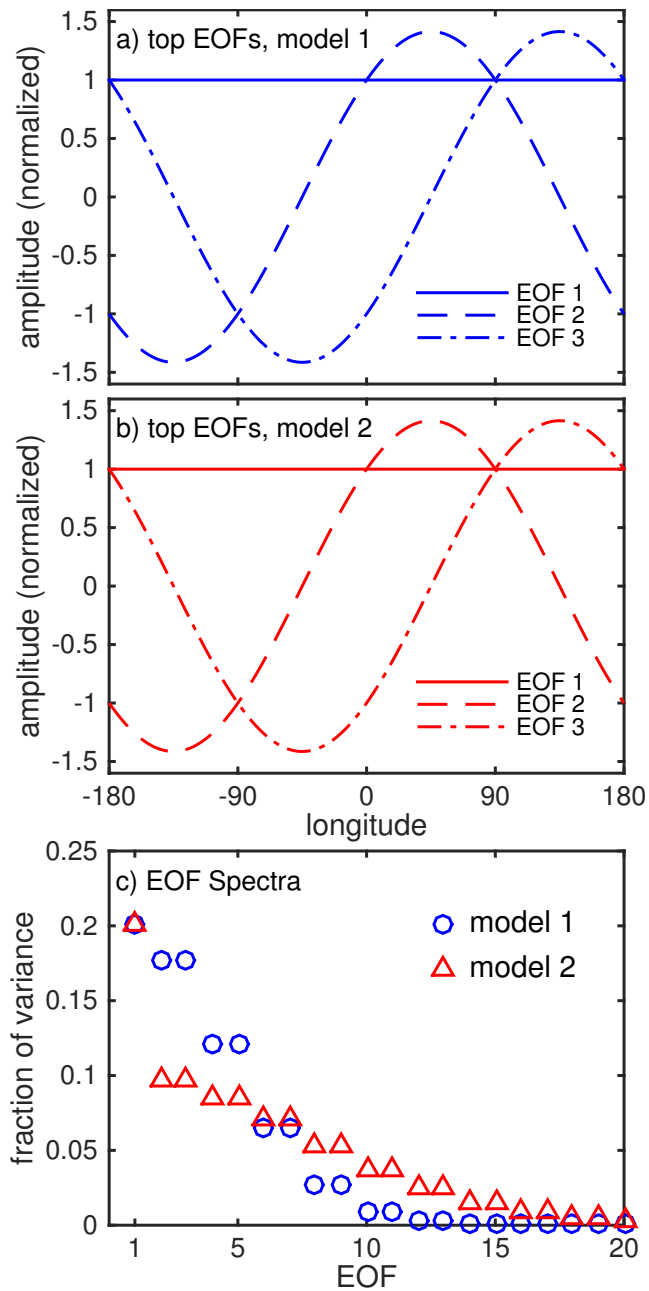


FIG. 2. The EOF structure of the two stochastic models. (a) and (b) show the top three EOFs for models 1 and 2, respectively, normalized to have unit variance. In the limit of infinite sampling, the EOF patterns from the two models are identical. (c) The models' EOF spectra, marking the fraction of the total variance associated with each of the top 20 EOFs.

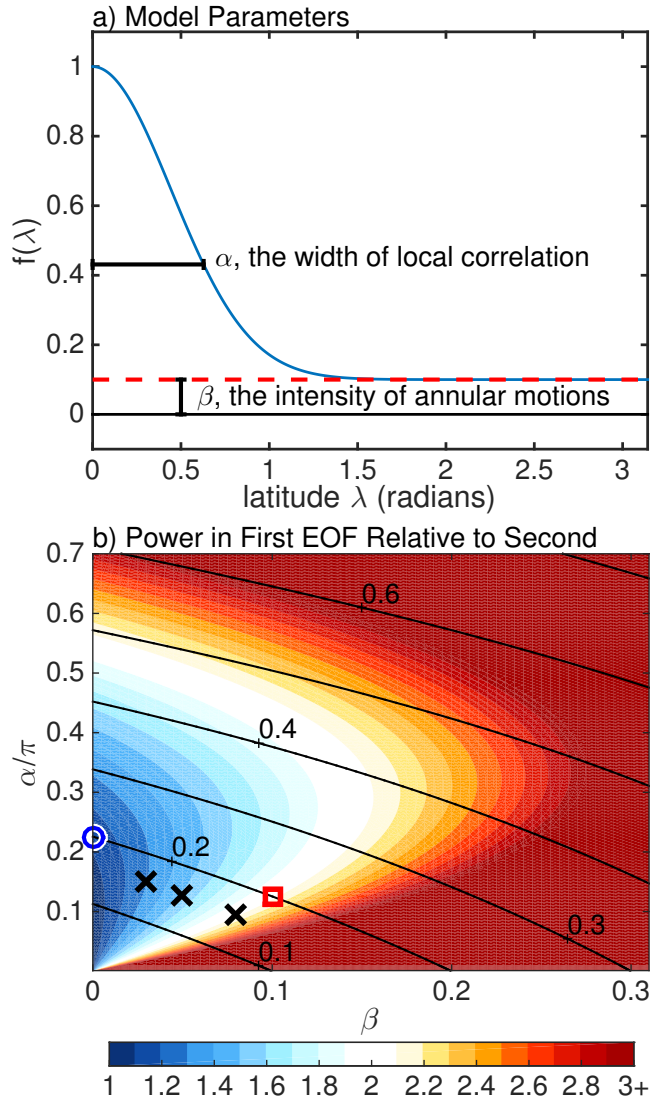


FIG. 3. The impact of local vs. annular correlation in the “Gaussian + baseline” family of stochastic models. (a) illustrates the parameters α and β which characterize the correlation function $f(\lambda)$ for each model. (b) maps out the variance expressed by the first EOF (black contours) and the ratio of the variance expressed by the first EOF to that of the second (color shading) as a function of α and β . The first EOF is always annular, and the second always a wavenumber 1 pattern. The blue and red markers show the location of models X_1 and X_2 (illustrated in Figs. 1 and 2) in parameter space, respectively; both fall along the same black contour, as their top EOF expresses 0.2 of the total variance. The black x’s will be discussed in the context of Fig. 11

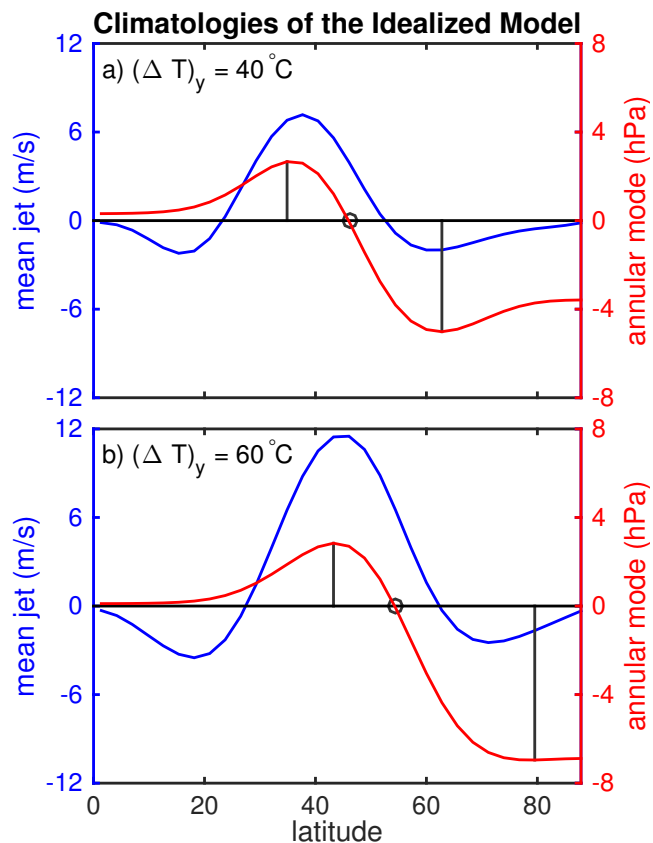


FIG. 4. The mean jet structure and annular modes of the Held and Suarez (1994) model for the (a) $(\Delta T)_y = 40$ and (b) $(\Delta T)_y = 60^\circ\text{C}$ integrations. The jet is characterized by the time mean 850 hPa winds (blue lines, corresponding with the left y-axes), and the annular mode is the first EOF of daily, zonal mean SLP (red, right y-axes), normalized to indicate the strength of 1 standard deviation anomalies. The latitudes of the node, equatorward and poleward lobes of the annular mode are highlighted, and correspond with the analysis in Fig. 5.

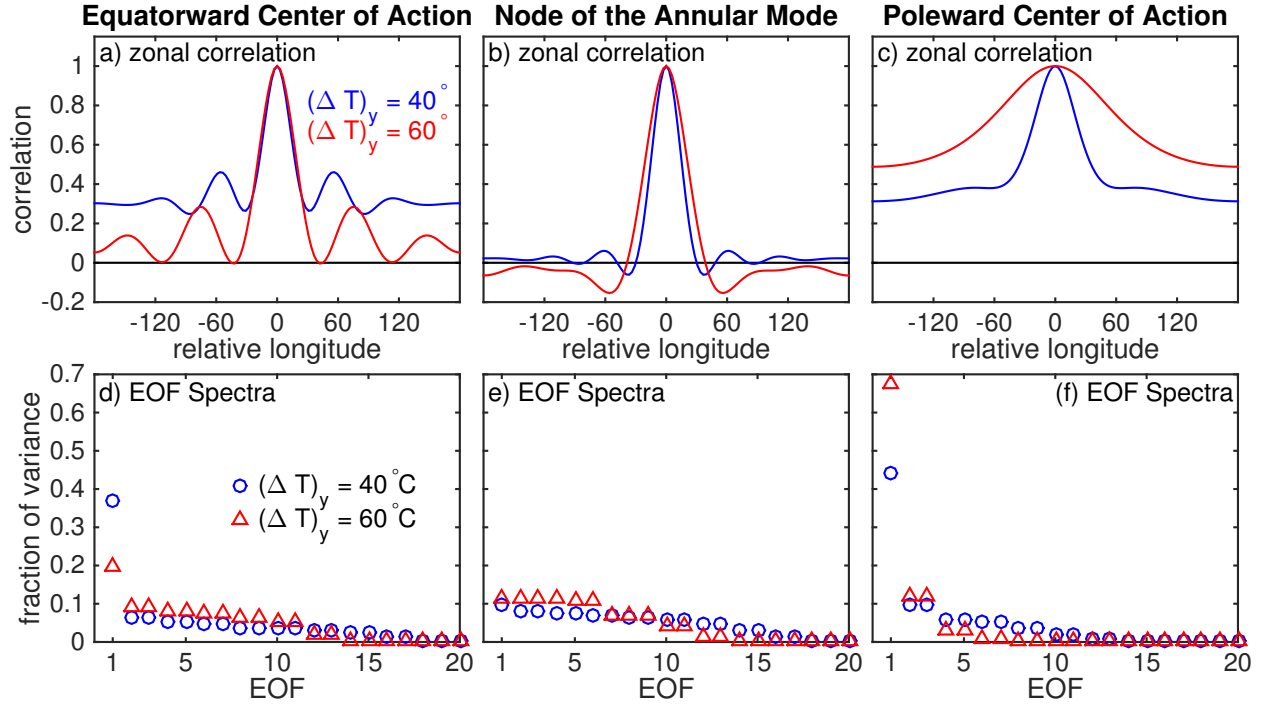


FIG. 5. Characterizing the zonal structure of 10 day pass filtered SLP anomalies in the Held and Suarez (1994) model. (a,d) and (c,f) show analysis based at the latitude of the equatorward and poleward centers of action of the annular mode, respectively, while (b,e) show analysis based at the nodes of the annular mode. (a,b,c) show the zonal correlation structure $f(\lambda)$ and (d,e,f) the fraction of variance associated with each of the top 20 EOFs for the integrations with (blue) $(\Delta T)_y = 40$ and (red) $(\Delta T)_y = 60^\circ\text{C}$.

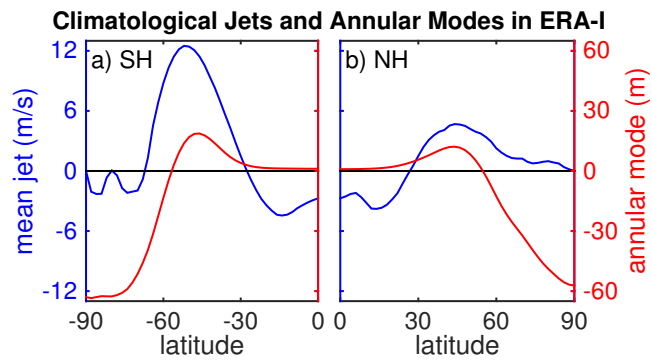


FIG. 6. The same as Fig. 4, but for the (a) Southern and (b) Northern Hemispheres in ECWMF Interim reanalysis, based on the period 1979-2013. To avoid interpolation over mountainous regions, the annular modes are defined in terms of daily, zonal mean 850 hPa geopotential height, Z_{850} , instead of SLP.

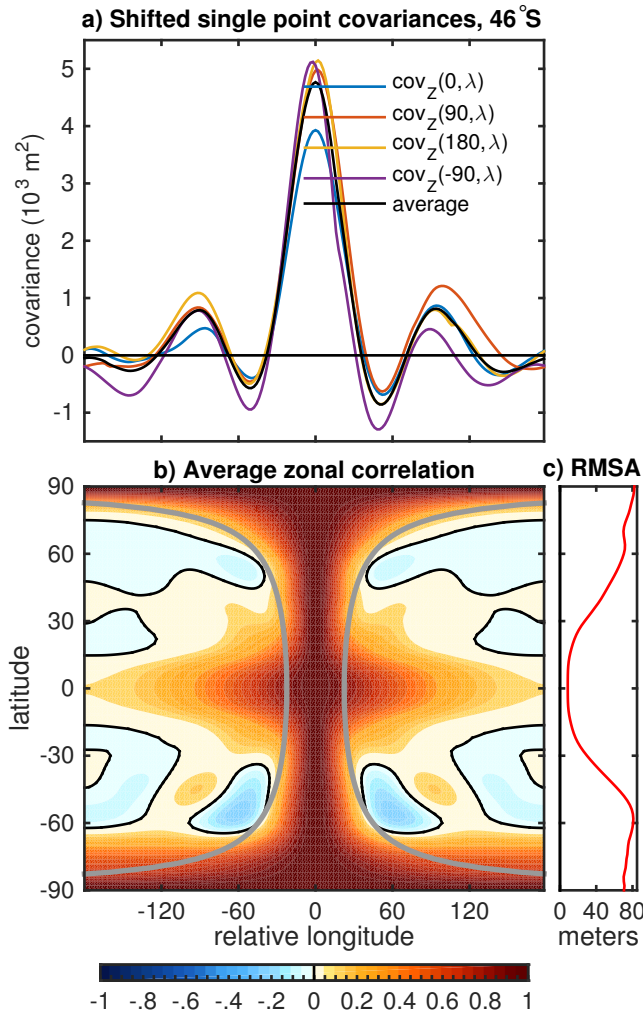


FIG. 7. Characterizing the longitudinal correlation structure of 10 day low pass filtered 850 hPa geopotential height in ERA-Interim. (a) Sample single point correlation maps at 46°S (the equatorward center of action of the SAM), shifted so that base points line up. The black line is the mean of the four curves, an “average single point correlation map”. (b) The average zonal correlation structure of 10 day low pass filtered Z_{850} as a function of latitude. The contour interval is 0.05, with black contours marking zero correlation, and gray lines indicate a separation of 5000 km, to provide a sense of geometry on the sphere. (c) The root mean square amplitude of 10 day low pass filtered Z_{850} anomalies.

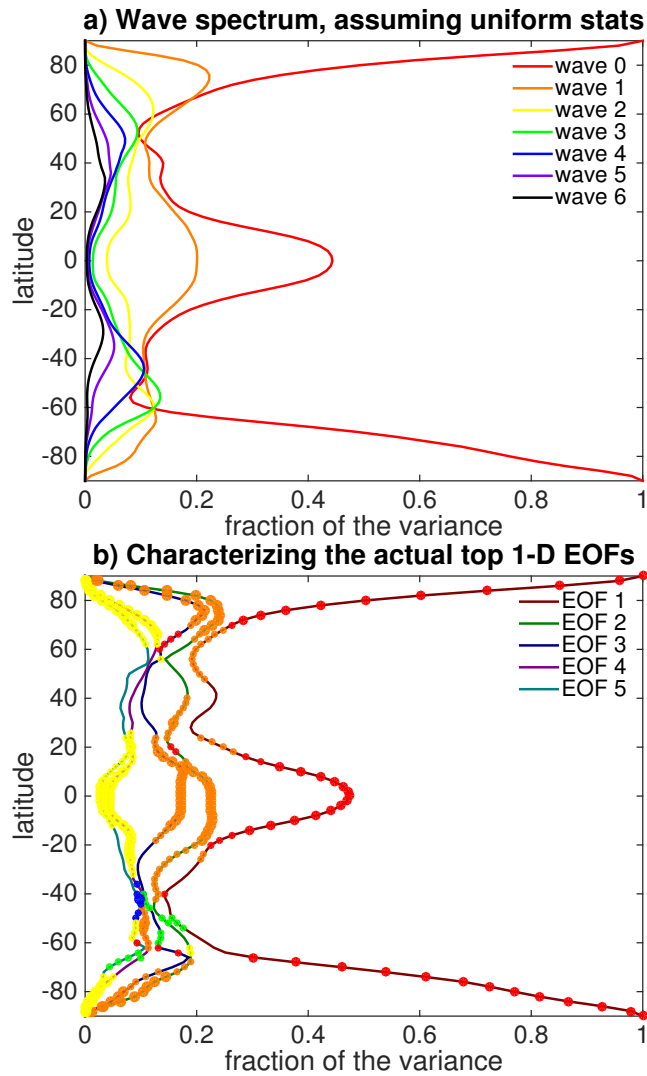


FIG. 8. A comparison of predictions based on zonally uniform statistics to the actual zonal EOF structure of 10 day low pass filtered Z_{850} . (a) For each latitude, the fraction of variance associated with wavenumbers 0 to 6, given the average zonal correlation structure in Fig. 7b and assuming zonally uniform statistics (see text for details). (b) Again for each latitude, the fraction of variance associated with the top five 1-D longitudinal EOFs, but now based on the full flow. Large (small) colored dots indicate when a given wavenumber dominates more than 75% (50%) of the power in the EOF, the color identifying the respective wavenumber with the color convention in (a), i.e., red=wave 0, orange=wave 1.

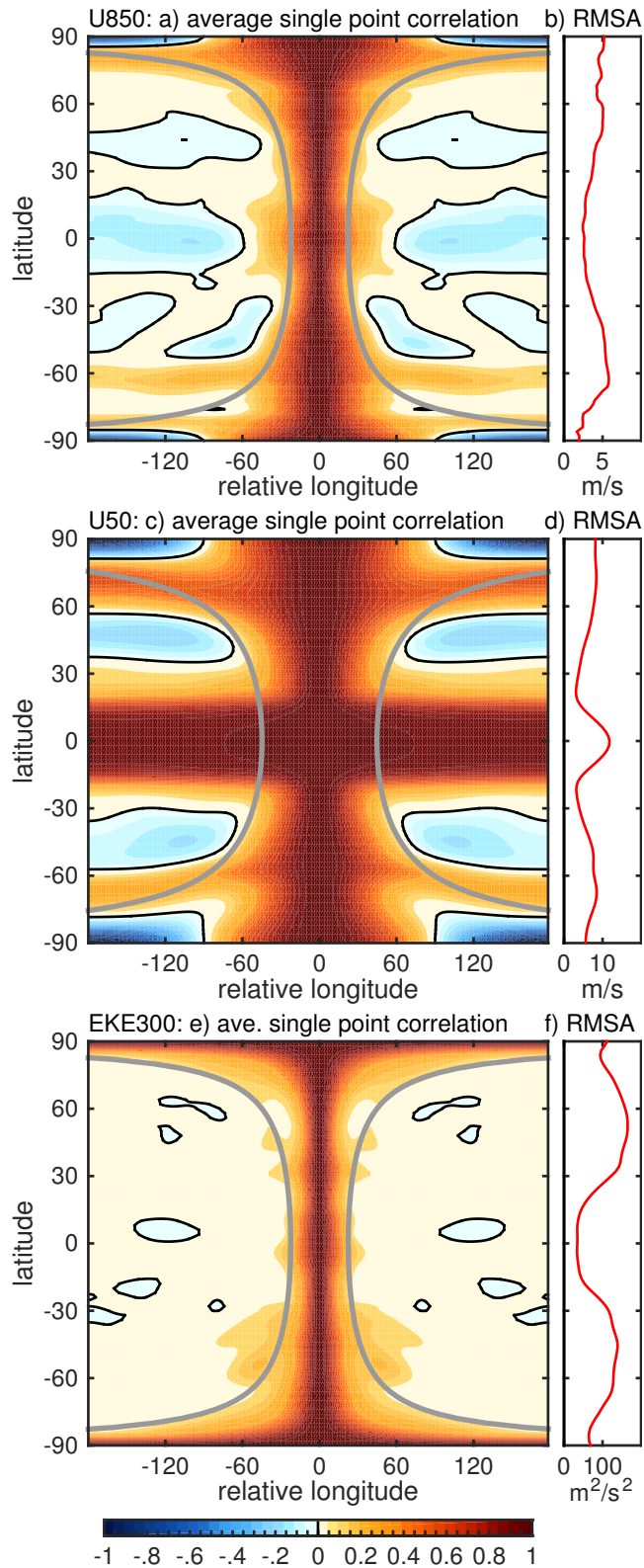


FIG. 9. The average correlation structure of (a) zonal wind at 850 hPa, (c) zonal wind at 50 hPa, and (e) eddy kinetic energy at 300 hPa. As in Fig. 7b, thin black contours mark zero correlation and the thick gray contours give a sense of sphericity, marking a separation of 5000 km as a function of latitude in (a) and (e) and a distance of 10000 km in (c). Panels (b), (d), and (f) show the root mean square amplitude of variations as a function latitude for each variable, respectively.

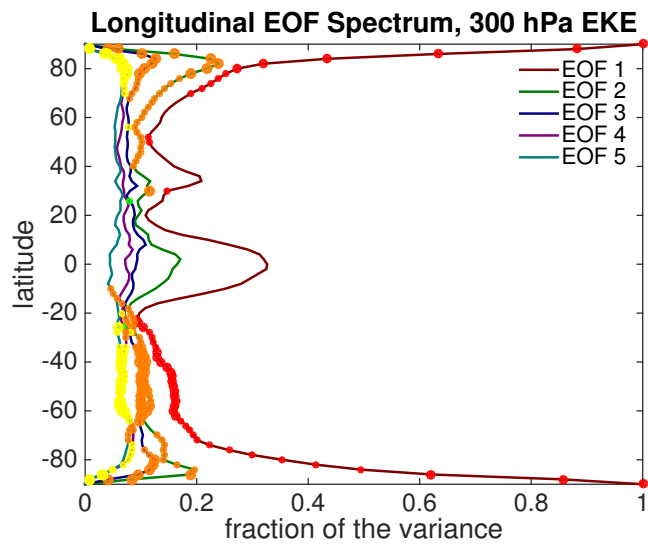


FIG. 10. The same as in Fig. 8b, but for eddy kinetic energy at 300 hPa. Zonal asymmetry in the statistics lead to substantial mixing between wavenumbers in the Northern Hemisphere (outside the polar cap) and tropics, such no single wavenumber dominates each EOF. Statistical annularity in the Southern Hemisphere, however, leads to a clearly order spectrum poleward of 25°S, dominated by an annular (wavenumber 1) mode at all latitudes.

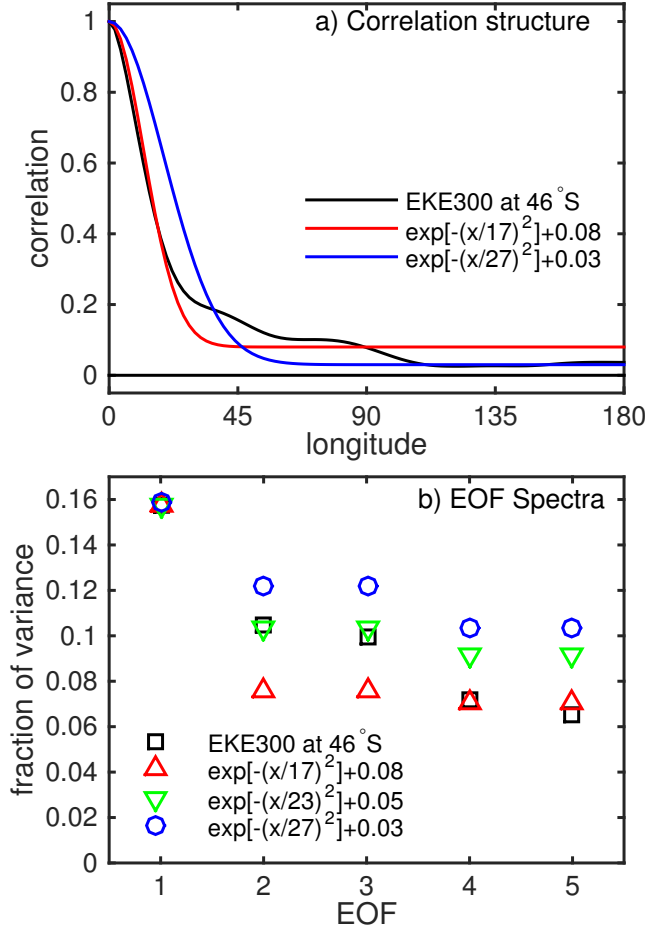


FIG. 11. (a) Comparison between the average longitudinal correlation structure of EKE_{300} at 46°S and two possible fits with the Gaussian + baseline model of Section 3. As detailed in the text, the first fit (red) is optimized to capture the initial decay in correlation, while the second fit (blue) is optimized for the long range correlation baseline. (b) The 1-dimensional EOF spectra of EKE_{300} at 46°S , compared against the spectrum for the two fits of the Gaussian + baseline model shown in (a), and a third model with parameters $\alpha = 23^\circ$ and $\beta = 0.05$, as discussed in the text.